Sensitivity and fragmentation calibration of the time-of-flight mass spectrometer RTOF on board ESA's Rosetta mission

Sébastien Gasc[a], Kathrin Altwegg[a,b], Björn Fiethe[c], Annette Jäckel[a], Axel Korth[d], Léna Le Roy[b], Urs Mall[d], Henri Rème[e], Martin Rubin[a], J. Hunter Waite[f], Peter Wurz[a]

[a]*Physikalisches Institut, University of Bern, Sidlerstrasse 5, CH-3012 Bern, Switzerland*
[b]*Center for Space and Habitability, University of Bern, Sidlerstrasse 5, CH-3012 Bern, Switzerland*
[c]*Institute of Computer and Network Engineering (IDA), TU Braunschweig, Hans-Sommer-Strasse 66, D-38106 Braunschweig, Germany*
[d]*Max-Planck-Institut für Sonnensystemforschung, Justus-von-Liebig-Weg 3, D-37077 Göttingen, Germany*
[e]*Institut de Recherche en Astrophysique et Planétologie, UPS, University of Toulouse and CNRS, Toulouse, France*
[f]*Space Science and Engineering Division, Southwest Research Institute, 6220 Culebra Road, San Antonio, TX-78228, USA*

Abstract

The European Space Agency's Rosetta spacecraft, with the Rosetta Orbiter Spectrometer for Ion and Neutral Analysis (ROSINA) onboard, has been following and observing comet 67P/Churyumov-Gerasimenko since summer 2014. Prior to this period, and due to a technical failure also during this period, optimisation and calibration campaigns have been conducted on ground with the Reflectron-type Time Of Flight (RTOF) mass spectrometer as a preparatory work for the analysis of data recorded during the science phase of the mission.

In this work, we show the evolution of the performance of RTOF, and demonstrate and quantify the sensitivity and functionality of RTOF onboard Rosetta. We also present a fragmentation and sensitivity database for the most abundant molecules observed around the comet such as H_2O, CO, CO_2, as well as the noble gases.

Keywords: Rosetta, ROSINA/RTOF, comet 67P/Churyumov-Gerasimenko, mass spectrometry, fragmentation pattern, sensitivity

1. Introduction

The thorough study of comet 67P/Churyumov-Gerasimenko (67P/C-G) by the European Space Agency's Rosetta spacecraft began in August 2014 as the probe arrived within 150 km from the nucleus. Since then, Rosetta followed 67P/C-G as it reached its perihelion and beyond, providing new insights about comets and how they are formed.

Among the eleven instruments carried by the orbiter, the Rosetta Orbiter Spectrometer for Ion and Neutral Analysis (ROSINA) has been designed to analyse the composition of the volatiles in the cometary atmosphere at the location of the Rosetta spacecraft. The science goals of ROSINA are to determine the global molecular, elemental, and isotopic composition of the cometary nucleus, and to investigate the temporal changes of the comet on its journey around the Sun. Furthermore, ROSINA aims as well to investigate the relationship between cometary and interstellar material and the implications for theories on the origin of the Solar System (Balsiger et al., 2007).

To achieve these goals, a three-sensor approach has been adopted: ROSINA consists of two mass spectrometers, the Reflectron-type Time Of Flight mass spectrometer (RTOF) and the Double Focusing Mass Spectrometer (DFMS), and a pressure sensor, the COmetary Pressure Sensor (COPS). With a total mass of 34.8 kg, ROSINA represents a little more than 20% of the Rosetta orbiter's payload. Complementing each other to be able to reach the scientific objectives, they also provide a necessary redundancy, due to the long mission duration. The unprecedented discoveries of ROSINA illustrate the importance of in situ measurements in space research (Altwegg et al., 2015; Rubin et al., 2015; Hässig et al., 2015; Bieler et al., 2015). Particularly, the study of the main compounds of the coma − such as H_2O, CO and CO_2 − from ground is highly limited due to near infrared absorption of the Earth's atmosphere (H_2O) or the small permanent electric dipole moments of the symmetric molecules (CO and CO_2) (Mumma and Charnley, 2011; Mall et al., 2016).

The primary goal of RTOF is to identify the species present in 67P/C-G's atmosphere and to investigate their temporal variation. To deconvolve a mass spectrum that results from a gas mixture, it is necessary to know the specific response of the mass spectrometer to each molecule. This response depends on the species dependent sensitivity of the instrument and the fragmentation of molecules inside the ion source. It is therefore necessary to perform an instrument-specific calibration, for as many species expected in the vicinity of the comet as possible. This article presents the current capabilities of RTOF, reduced after two technical failures which occurred in flight, and describes the calibration procedure followed to characterize RTOF, as a preparatory work for the data interpretation.

Email address: sebastien.gasc@space.unibe.ch (Sébastien Gasc)

2. Materials and Methods

2.1. Time-of-flight mass spectrometry

Compared with other types of mass spectrometry, time-of-flight (TOF) mass spectrometry has the advantage of being able to record all gas species simultaneously, with a high mass range together with a high temporal resolution. TOF mass spectrometers are therefore natural candidates for the in situ study of volatiles and organic compounds in the vicinity of a comet like 67P/C-G.

The principle of a TOF mass spectrometer is to ionize the gas to be analysed, to accelerate the created ions with the same energy qU so that their speed v would only depend on their mass per charge m/q (Eq. (1)), and to measure the time $t = d/v$ they need to travel through the instrument before they are detected (Eq. (2)).

$$qU = \frac{1}{2}mv^2 \tag{1}$$

$$t = d \cdot \sqrt{\frac{m}{2qU}} \tag{2}$$

Starting from Eq. (2), one can derive Eq. (3) linking the mass to the time of flight of the ions:

$$m = \left(\frac{t - t_0}{C}\right)^2 \tag{3}$$

where C and t_0 are constant parameters whose computation will be detailed in Section 2.8.1.

The ionization takes place in an ion source and is usually performed through electron impact: a filament is heated and emits electrons, which are then accelerated into the ionization zone with an energy of $qU = 70$ eV. The majority of ionization cross sections for organic molecules have their maxima in this energy range (Mark, 1982). The newly created ions are extracted towards a drift tube by a high-voltage pulse with a duration of typically a few μs and at a frequency of typically a few kHz, which varies depending on the mass range to be reached: at high extraction frequencies, the heavy ions do not have enough time to fly through the instrument before a new extraction occurs. A detector located at the end of the drift tube measures the arrival time of the ions, from which we can deduce the flight time t of the ions.

The ions formed in the ion source have an initial kinetic energy distribution. Ions with the same mass may therefore not have the same speed and arrive at different times, decreasing the mass resolution of the instrument – the mass resolution being defined as $m/\Delta m$, where Δm is the full width of the peak measured at 50% of the peak height. A good way to lessen this phenomenon was first proposed by Mamyrin et al. (1973): an ion mirror (reflectron) makes the ions turn around at the end of the drift tube and focuses them in a time-focus plane on the detector (see Fig. 1). The first advantage of using a reflectron is the compensation of the energy dispersion: faster ions penetrate deeper into the reflectron and hence have a longer way such that they arrive at the detector at the same time as the slow ones. Secondly, the flight path is also doubled, increasing the mass resolution of TOF mass spectrometers equipped with a reflectron. Finally, the reflectron can be designed to also geometrically focus the ions onto the detector to maximise the ion-optical transmission (Scherer et al., 2006). RTOF belongs to this category of reflectron-type TOF mass spectrometers.

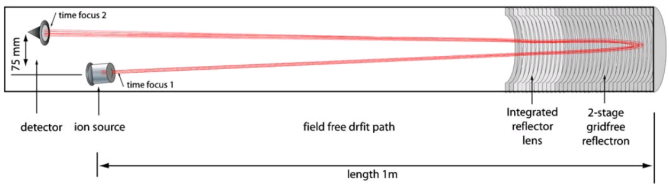

Figure 1: Principle of a TOF mass spectrometer equipped with a reflectron (picture based on Scherer et al. (2006)).

2.2. RTOF

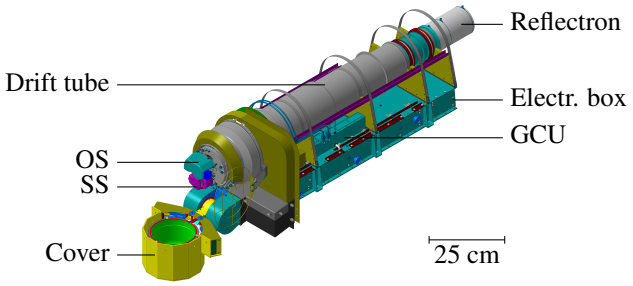

Figure 2: 3D drawing of RTOF. Aboard Rosetta, the drift tube, the reflectron, and the electronic box – the elongated structure below the ion optical system – remain inside the spacecraft, only the cover and the entrances of the SS and of the OS remain outside.

RTOF contains two ion sources (see Fig. 2): the Storage Source (SS) and the Orthogonal Source (OS). Both are capable of measuring cometary neutral gas while the latter also allows measuring cometary ions. They can be operated independently or together to study neutrals and ions simultaneously. In the SS, between two subsequent extraction pulses, the ions are stored between the backplane of the source and the extraction grid where the extraction pulse is applied (see Abplanalp et al. (2010)). With this ion storage, it is possible to detect a large fraction of the ions constantly produced in the ionizing portion of the SS, thus effectively reducing the duty cycle.

The drift tube is 83 cm long, giving an effective flight path between the ion source and the detector of 2.2 m thanks to the reflectron. During their flight, the ions have a typical energy of 1 keV.

In its original design, RTOF had a mass resolution greater than 5000 at 50% peak height, and the ability to detect ions up to 2000 u/e (Scherer et al., 2006; Balsiger et al., 2007). However, after a successful in-flight switch on of RTOF during the commissioning phase in 2004, a failure in the main 9 kV high voltage converter occurred, due to outgassing in the nearby potting. This outgassing lead to partial discharges along some of the potted cables. After long investigations and numerous tests in the laboratory with the ground instrument, a software solution was implemented and made possible to operate RTOF, but

at significantly lower voltages for the ion-optical system and therefore with lower performance.

Optimisations have been conducted on the ground during the hibernation of Rosetta from 2011 to 2014 (Bieler et al., 2011), and in space after its wake up in January 2014. They consisted in tuning the potentials of the ion source, the reflectron, and the MCP, and allowed RTOF to reach in June 2015 a mass resolution of approximatively 500 at 50% peak height (mass 28) and a mass range going from 1 u/e to 1150 u/e. The temporal resolution remained unchanged at 200 s. Later, on 27/05/2015, a failure of the main SS filament required the use of the redundant filament, and optimisations for the SS had to be extended after June 2015 and until December 2015, to reach similar performance as with the main filament.

Table 1 defines different periods for the optimisation steps (both sources), and Fig. 3 shows the evolution of the mass resolution and the signal-to-noise ratio (SS only).

Table 1: Optimisation periods for the SS and the OS. Steps 3a and 3b for the SS correspond to the same settings. The settings for period ⋆ were never set permanently in flight due to a failure of the main SS filament on 27/05/2015. Periods 5 to 7 therefore refer to optimisations conducted with the redundant filament of the SS. Values for C and t_0 are given here as starting points.

Ion source	Period	Start time	C [× 1.65 ns·u$^{-0.5}$]	t_0 [×1.65 ns]
SS	1	24/04/2014	3165.7752	26.9347
	2	03/09/2014	3104.1533	29.1291
	3a	03/10/2014	3126.5185	27.2657
	4	08/04/2015	3116.2918	37.6121
	3b	11/05/2015	3126.5185	27.2657
	⋆	–	3130.7999	27.5732
	5	05/06/2015	3119.1502	26.3378
	6	05/11/2015	3139.7935	40.2345
	7	03/12/2015	3124.7623	27.7889
OS	1	24/04/2014	3092.4879	29.0694
	2	17/10/2014	3055.0910	28.2969

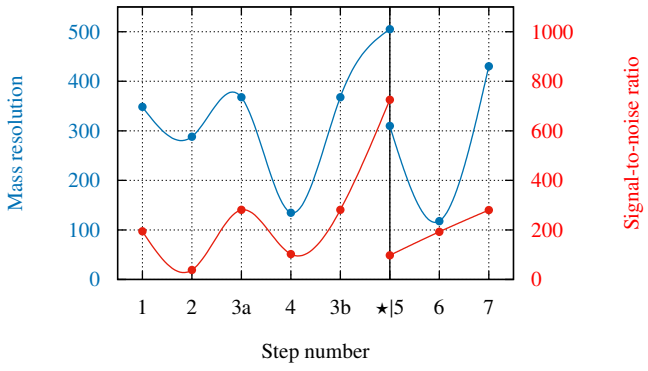

Figure 3: Evolution of the mass resolution and the signal-to-noise ratio of the SS for the periods defined in Table 1. Step ⋆|5 corresponds to the failure of the main SS filament and the switch to the redundant SS filament. No curve is shown for the OS as its settings were changed only twice.

2.3. Calibration's motivation

The ionization process occurring in the ion sources results in a fragmentation of the analysed molecules. Depending on the ionization conditions, each species has its own characteristic fragmentation pattern, which depends on the electron energy. This requires specific calibration. Hence, in this work, the RTOF laboratory model on ground has been used to study the main constituents in the coma of a comet, that is H_2O, CO, and CO_2 (Bockelée-Morvan et al., 2004), as well as the noble gases He, Ne, Ar, Kr, Xe, which are key compounds to study the origin of volatiles of the inner planets (Owen et al., 1992); in addition, the noble gases do not fragment, which is another advantage to understand the sensor. We know from the calibrations on the ground that the geometry and operation parameters for the flight and the flight-spare are almost the same. Differences are known accurately enough to consider the fragmentation pattern as identical for both instruments. Potential differences are taken into account in the error estimation.

The SS and the OS have different ion-optical designs, and the voltages applied in the ion sources have been optimized independently. It is therefore expected to get different results between the two ion sources. A comparison will be made with the National Institute of Standards and Technology (NIST) database of fragmentation patterns (Stein, 2013), although it is not required to get here the same results as NIST as there are sensor specific factors to be considered.

2.4. Acquisition system

The signal acquired in the two ion sources is amplified by two Micro-Channel Plates (MCP) (Schletti et al., 2001), and processed by two acquisition boards: the Equivalent Time Sampler (ETS) for the SS, and a simplified board for the OS, the ETS-Light (ETSL). Both data acquisition systems serve as Time to Digital Converters (TDC), recording the time when the signal exceeds a programmable trigger level; in addition, the ETS also samples each peak with an Analog to Digital Converters (ADC) system. Since the signal levels in the OS are small, such an *event* can be interpreted as a single ion when the density is low enough to consider that only one ion is hitting the detector in a time sampling bin. For the SS though, the ion density is supposed to be much higher due to the ion storage capability and leads to multiple ions arriving at the same time on the detector. To prevent an underestimation, the ETS system is also capable of converting the signal height into a digital value, or *histogram*, using 16 high speed, low power ADC fired with a 1.65 ns delay after trigger, consequently giving a time resolution for the ETS of 1.65 ns.

These 16 ADC do not all respond the same way, and create a pattern observed in the histogram data with a 16 × 1.65 ns repetition. This pattern can be filtered with a specific factor for each ADC, calculated for instance by summing the contribution in a spectrum of each ADC individually, and then normalizing these sums to obtain a correction factor to apply on each ADC. An example of this filtering is shown Fig. 4.

The ratio *histogram* / *events* is of high importance to estimate whether more than one ion hits the detector at the same time.

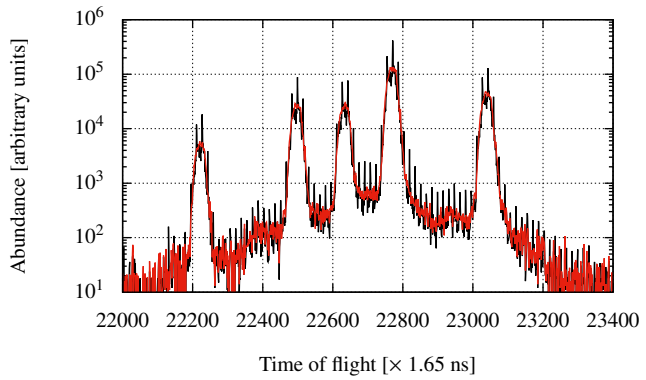

Figure 4: ADC correction (red) applied on a SS spectrum (black) acquired with a gas inlet of krypton (zoom on the main krypton isotopes).

If the ratio remains constant for the low intensity peaks as well as the high intensity peaks, then it is reasonable to consider that one event corresponds to one ion (this is the case in Fig. 5). In that case, the ratio gives then the number of counts of the ADC which correspond to the signal of one ion. If the ratio increases for a high number of counts, then more than one ion is contained in the signal, which can be calculated from the ratio determined at lower signals. The behaviour of the histogram to events ratio has been carefully monitored during the measurements detailed hereafter, especially the ones in the highest pressure range.

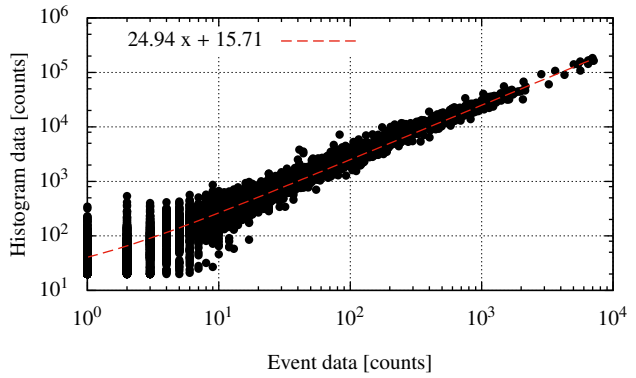

Figure 5: Constant histogram to event ratio, indicating that the peaks with the highest intensities are most probably not underestimated.

2.5. RTOF operation

RTOF has several operation modes to ensure optimized scientific data acquisition. For each source, three different extraction frequencies are possible – 10 kHz, 5 kHz, and 2 kHz – and three different filament emissions are available – 20 μA, 100 μA, and 200 μA. A few characteristics of the modes are listed in Table 2. All modes accumulate ions for either 200, 400, or 600 seconds which then gives the time resolution of two subsequent measurements. In this study, the 2 kHz extraction modes (M0528 & M0529) have not been calibrated.

Table 2: RTOF neutral modes calibrated in this work (except SS-M0528 and SS-M0529).

Ion source & Operation mode	Extraction frequency	Filament emission	Acqu. time [s]	Mass range
SS – M0501	10 kHz	20 μA	200	1 – 120
SS – M0506	5 kHz	20 μA	200	1 – 520
SS – M0511	10 kHz	100 μA	200	1 – 120
SS – M0516	5 kHz	100 μA	200	1 – 520
SS – M0521	10 kHz	200 μA	200	1 – 120
SS – M0522	10 kHz	200 μA	400	1 – 120
SS – M0526	5 kHz	200 μA	200	1 – 520
SS – M0527	5 kHz	200 μA	400	1 – 520
SS – M0528	2 kHz	200 μA	400	50 – 1150
SS – M0529	2 kHz	200 μA	600	50 – 1150
OS – M0513	10 kHz	100 μA	200	1 – 130
OS – M0523	10 kHz	200 μA	200	1 – 130
OS – M0524	10 kHz	200 μA	400	1 – 130
OS – M0543	5 kHz	100 μA	200	1 – 550
OS – M0553	5 kHz	200 μA	200	1 – 550
OS – M0554	5 kHz	200 μA	400	1 – 550

2.6. Calibration facility

RTOF has been operated in the CAlibration SYstem for the Mass spectrometer Instrument ROSINA (CASYMIR), shown in Fig. 6. This facility has been designed to reproduce the conditions expected in the coma of the comet (Graf et al., 2004).

Calibration can be done either with residual gas only or with a specific gas mixture, produced in a gas mixing unit. An inlet system has been added specifically for this calibration campaign to study liquid and solid compounds; it consists of a glass tube which can be easily pumped, homogeneously heated, and exchanged with tubes containing other compounds.

Particle densities range between 10^{13} and 10^{17} m^{-3}. Nine pressure sensors ensure the monitoring of the pressure between the gas mixing unit and RTOF. A thermal valve was used to keep the inlet pressure stable, based on the pressure sensor located the closest to the inlet system.

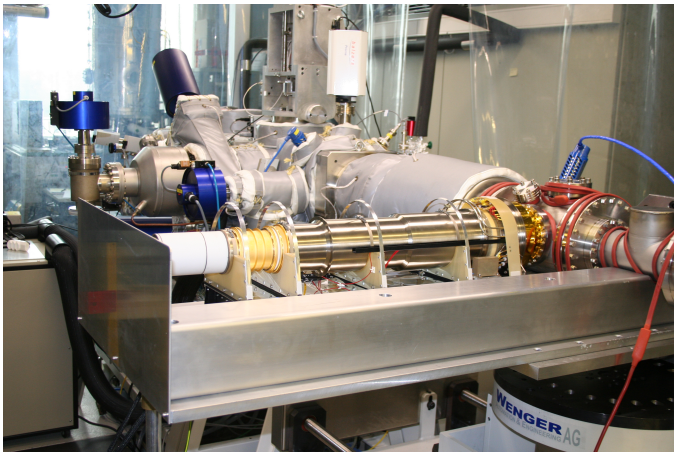

Figure 6: Picture of RTOF (front) connected to CASYMIR (back). The RTOF source entrances are aligned with the docking section of CASYMIR on the right side of the picture.

2.7. Measurement procedure

Three different partial pressures were set for each species, ideally at 10^{-7} mbar, 10^{-8} mbar, and 10^{-9} mbar. The pressure measurements were recorded using a Granville-Phillips ion gauge (Granville-Phillips, 2007), and the measurement procedure for both RTOF sources is described below.

RTOF was switched ON and running for 1.5 h before the first calibration measurement to allow for good outgassing of the ion source, and to reach thermal equilibrium in the sensor and its electronics together with the calibration chamber. Once the equilibrium was reached, background measurements of the residual gases in the chamber were acquired for each of the operation modes described in Table 2. Each of the operation modes was then acquired three times while the gas inlet was open and the pressure was regulated by a thermal valve; this step was performed for the three pressure ranges mentioned above. Finally, background measurements of the residual gases in the chamber were once more acquired after a waiting time of 30 minutes after closing the inlet valve for each of the operation modes.

2.8. Data treatment

2.8.1. Mass scale

The first step for the identification of peaks in a spectrum is to apply a mass scale on the time axis, using Eq. (3). The conversion from time to mass requires the calculation of two parameters, C and t_0, which are calibration constants that can be calculated according to Eq. (4) and Eq. (5), provided that at least two peaks can already be identified (see also Scherer et al. (2006)). The use of multiple mass lines averages the individual errors, making the application of the mass scale more robust (an evaluation of this method is available in Riedo et al. (2013), Fig. 11). For instance, for the krypton spectra acquired with SS in mode M0521, the mass scale was applied using four reference peaks as shown in Table 3 (the krypton isotopes are shown in Fig. 4).

$$C = \frac{N \sum_{i=1}^{N} t_i^2 - \left(\sum_{i=1}^{N} t_i \right)^2}{N \sum_{i=1}^{N} \left(\sqrt{m_i} t_i \right) - \sum_{i=1}^{N} \sqrt{m_i} \sum_{i=1}^{N} t_i} \tag{4}$$

$$t_0 = \frac{\sum_{i=1}^{N} \left(\sqrt{m_i} t_i \right) \sum_{i=1}^{N} t_i - \sum_{i=1}^{N} \sqrt{m_i} \sum_{i=1}^{N} t_i^2}{N \sum_{i=1}^{N} \left(\sqrt{m_i} t_i \right) - \sum_{i=1}^{N} \sqrt{m_i} \sum_{i=1}^{N} t_i} \tag{5}$$

N is the number of reference peaks ($N \geqslant 2$), t_i the time of flight of the i^{th} peak, and m_i its associated theoretical mass. The theoretical masses are calculated using the Commission on Isotopic Abundances and Atomic Weights (CIAAW) database (where the atomic masses are adapted from Wang et al. (2012)); the mass of an electron has been subtracted, and the peak position is determined using a pseudo-Voigt profile fitting as described in the next section.

Small variations of C and t_0 are possible between two spectra due to several effects such as the temperature of the electronics. Larger variations are encountered when the settings of the instrument are modified, giving different flight times for the ions. For the SS, with the reference peaks in Table 3, and for the krypton measurements, $C = 4095.80$ ns·u$^{-0.5}$ and $t_0 = 50.8113$ ns.

Table 3: Time of flight of the four reference peaks used for the calculation of C and t_0. The deviation represents the difference between the theoretical mass and the mass re-calculated according to C and t_0.

i	Reference peak	Theoretical mass m_i [u]	Time of flight t_i [ns]	Deviation [ppm]
1	H_2, residual	2.0151	5865.2	−92
2	H_2O, residual	18.0100	17432.2	56
3	CO_2, residual	43.9893	27216.1	−9
4	^{84}Kr, gas inlet	83.9109	37569.6	−4

2.8.2. Fragmentation patterns

The determination of the fragment distribution requires the calculation of the area under each peak, performed with a pseudo-Voigt profile fit (Eq. (6) to (8)), using the least squares method.

$$V_p(x) = \eta \cdot L(x) + (1 - \eta) \cdot G(x) \tag{6}$$

$$G(x) = A_0 \exp\left(-\frac{(x - x_0)^2}{2\sigma^2} \right) \tag{7}$$

$$L(x) = \frac{A_0}{1 + \frac{(x - x_0)^2}{2\sigma^2}} \tag{8}$$

In the equations (6) to (8), $V_p(x)$ is the pseudo-Voigt function, defined as a linear combination of a Gaussian function $G(x)$ and a Lorentzian function $L(x)$. η is an integer which determines the participation of $G(x)$ and $L(x)$ in $V_p(x)$, A_0 is the amplitude of the peak, x_0 its position, and σ the Gaussian RMS width.

The fitting is done either independently when the peak is clearly separated from its neighbours, or together with the closest neighbour peaks in the cases of krypton and xenon for instance, where an overlap of the isotopes can be observed.

Depending on the settings of the instrument, this theoretical peak shape may change and requires the establishment of a modified fit function. As an example, Fig. 7 shows the overlap of the singly charged xenon isotopes, where all the peaks were fitted together. The peak at mass 28 was used to established the peak shape, which in this case consists of the sum of a pseudo-Voigt profile and 8 Gaussian functions to reproduce the left part of the peak.

After correcting the ADC pattern and applying a mass scale, all the peaks in the background spectra were fitted and numerically integrated to be subtracted from the subsequent calibration measurements obtained with the desired gas mixture. The error bars take into account the possible presence of residual air in the sample tube.

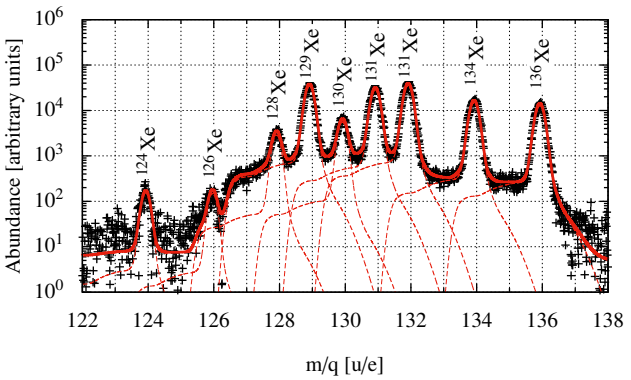

Figure 7: Overlap of the xenon isotopes, influencing the area under the neighbouring peaks, and therefore fitted together using the same peak shape, defined using the isolated peak on mass 28. The solid red line shows the sum of the 9 peaks fitted together; each individual peak is represented with a dashed line. An offset due to the electronic noise has been added to the fit function. This model is only shown as an example as the peak shape may change depending on the instruments settings. The ADC correction has already been applied.

2.8.3. Sensitivities

The sensitivity of a mass spectrometer to different species is needed to correctly convert measured counts to a physical unit. It depends on the cross section of the atom or molecule analysed, the detector efficiency, the filament emission, and the transmission of the instrument (Wurz et al., 2007).

The sensitivity is defined as:

$$S_i = \frac{I_j}{n_i \, f_{i\to j} \, I_{em}} \tag{9}$$

where i refers to the parent and j to one of the fragments, I_j is the ion current on the detector generated by the measured fragment, I_{em} the emission current, S_i the sensitivity for the gas i, and n_i the neutral density. $f_{i\to j}$ is the absolute fragmentation or isotopic ratio defined as:

$$f_{i\to j} = \frac{Q_{i\to j}}{\sum_j Q_{i\to j}} \tag{10}$$

with $Q_{i\to j}$ the relative fragmentation or isotopic fraction given in Table 4. As an example, $Q_{CO_2\to CO} = 9.73\%$, leading to $f_{CO_2\to CO} = 0.079$.

For each species, the sensitivity was deduced from the ratio $I_i/(I_{em}\, n_j)$ at three pressure ranges. The Granville-Phillips ion gauge used for the density measurements has an accuracy of 4 to 6% (Granville-Phillips, 2007), leading to an uncertainty in the sensitivity values of about 8%.

2.9. Normalization of the mass spectrometers data to COPS

To get accurate density values for mass spectra recorded in space, it is necessary to calibrate the relative densities from RTOF with the total density provided by COPS. This is due to the fact that the laboratory model and the flight model have different detector efficiencies and different threshold levels for the TDC; in addition, a change in detection sensitivity over the course of the mission is possible as well due to detector ageing or changes in electronics. In the following, a uniform approach for both mass spectrometers is presented to normalize the densities from RTOF and DFMS to COPS. These densities are the combination of the cometary signal and the spacecraft background; the latter will be removed later on. For more information on the spacecraft background, the reader is referred to Schläppi et al. (2010).

The calculations hereafter are based on the fact that the density measured by COPS is calibrated relative to molecular nitrogen N_2. Assuming that the coma is dominated by H_2O, CO, and CO_2, the COPS density is equal to the sum of the major species in the coma:

$$n_{COPS} = \frac{n_{H_2O}}{\beta_{H_2O}} + \frac{n_{CO}}{\beta_{CO}} + \frac{n_{CO_2}}{\beta_{CO_2}} \tag{11}$$

where β is a scale factor relative to N_2, reflecting the different ionization probabilities. Values below are from Granville-Phillips (2007):

$$\beta_{H_2O} = 0.893$$
$$\beta_{CO} = 0.952$$
$$\beta_{CO_2} = 0.704$$

Individual densities for RTOF and DFMS can be defined as:

$$n_i = \frac{a \cdot c_i}{S_i \cdot f_{i\to j}} \tag{12}$$

a: constant including all parameters which are sensor dependent but independent of the species
S_i: species, sensor, and emission dependent sensitivity
c_i: number of ions on detector in 20 s (DFMS) or 200, 400, or 600 s (RTOF), gain corrected

The contribution from the fragmentation of CO_2 in CO needs to be removed from the measured signal of CO:

$$n_{CO} = \frac{a \cdot c_{CO}}{S_{CO} \cdot f_{CO\to CO}} - n_{CO_2} \cdot f_{CO_2\to CO}$$

We now define the ratios of the densities relative to H_2O, which are independent of any degradation of the sensors (a vanishes):

$$r_{CO_2} = \frac{n_{CO_2}}{n_{H_2O}} = \frac{c_{CO_2} \cdot S_{H_2O} \cdot f_{H_2O\to H_2O}}{c_{H_2O} \cdot S_{CO_2} \cdot f_{CO_2\to CO_2}} \tag{13}$$

$$r_{CO} = \frac{n_{CO}}{n_{H_2O}} = \frac{c_{CO} \cdot S_{H_2O} \cdot f_{H_2O\to H_2O}}{c_{H_2O} \cdot S_{CO} \cdot f_{CO\to CO}} - r_{CO_2} \cdot f_{CO_2\to CO} \tag{14}$$

Starting from Eq. (11) and with the ratios defined above, one can finally derive the H_2O, CO, and CO_2 densities from Eq. (15), (16), and (17) respectively:

$$n_{H_2O} = \frac{n_{COPS}}{\frac{1}{\beta_{H_2O}} + \frac{r_{CO}}{\beta_{CO}} + \frac{r_{CO_2}}{\beta_{CO_2}}} \tag{15}$$

$$n_{CO} = r_{CO} \cdot n_{H_2O} \tag{16}$$

$$n_{CO_2} = r_{CO_2} \cdot n_{H_2O} \tag{17}$$

These densities are still a combination of the cometary signal and of the spacecraft background, therefore the spacecraft background has to be subtracted for each species individually.

3. Results

The results of the calibration campaign will be presented in this section and are valid for all the periods mentioned in Table 1, except for period 4: unlike the other steps, the ion source voltages were significantly changed during this period, modifying the electron beam energy and therefore the ionization probability and finally the fragmentation pattern. For all the other periods, fragmentation patterns are the ones presented in this article; sensitivity values are valid as well, however only relative to each other: the calculation of absolute densities for RTOF requires the calibration of the relative sensitivity-corrected densities of RTOF with the total density provided by COPS, as detailed in section 2.9.

3.1. Fragmentation and isotopic ratios

The fragmentation pattern and isotopic ratios obtained in this calibration campaign are summarized in Table 4. These results and the following discussion concern all the modes detailed in Table 2, as no significant difference in fragmentation could be observed between the three filament emissions, nor between the different extractions frequencies as should be the case.

3.1.1. H_2O, CO, and CO_2

Comparing our results with the literature (the CIAAW and the NIST databases) requires to consider the isotopologues of a species on one hand – such as HDO^+ and $H_2^{18}O^+$ for H_2O, $^{13}CO^+$ for CO^+, and $^{13}CO^+$, $^{13}CO_2^+$, and $C^{18}OO^+$ for CO_2^+ – and all the other fragments on the other hand.

Regarding the isotopologues mentioned above, the abundances obtained in this calibration campaign are in agreement with NIST, whose values are lying within the error bars of our calibration measurements.

However, and as expected, the fragmentation patterns differ for the SS and the OS. The ionisation in the SS occurs between the backplane and the extraction grid, where the pulse is applied, whereas in the OS the ionisation is done in the ion-optical system, in front of the backplane and of the extraction grid. This difference leads to an overall higher amount of fragments for the SS than for the OS – beside, once more, for the isotopologues.

A main difference with the literature is the presence of the water fragments H^+ and H_2^+; these two fragments do not appear in the NIST database. An explanation can be found in the nature of the mass spectrometer used by NIST – a quadrupole – for the establishment of their database: if the sensitivity of a time-of-flight mass spectrometer remains independent of the mass until $m \approx 200$ u/e, a typical quadrupole mass analyser offers a high sensitivity for masses between ≈ 15 u/e and 80 u/e, and a lower sensitivity otherwise. The higher abundance of fragments with light masses is consistent with this hypothesis.

Additionally, H_2^+ was not expected due to the lack of recombination at such low pressures and for such a short time – between their creation and the time they hit the MCP, the ions survive for 500 μs in the best case – but a peak at mass 2 is clearly visible in the spectra generated in the SS. This is probably due to chemical reactions in the source during the storage time.

Table 4: Fragmentation fractions for H_2O, CO, and CO_2, and isotopic abundances for the noble gases. Literature values are from the CIAAW database (Meija et al., 2016) for the isotopic ratios of the singly charged noble gases, and from NIST otherwise. Errors are calculated based on the fit error and the error on the density measurement.

Parent Daughters, isotopes	Mass / charge [u/e]	Fragmentation fraction [%] SS	OS	Lit. [%]
H^+	1.0073	13.02 ± 0.91	6.80 ± 1.34	∅
H_2^+	2.0151	0.80 ± 0.30	0.09 ± 0.08	∅
O^+	15.9944	1.34 ± 0.82	1.15 ± 0.06	0.90
OH^+	17.0022	23.34 ± 1.03	23.73 ± 0.42	21.22
H_2O^+	**18.0100**	**100.0 ± 2.7**	**100.0 ± 0.8**	**100.0**
HDO^+	19.0163	0.61 ± 0.15	0.54 ± 0.04	0.50
$H_2^{18}O^+$	20.0143	0.27 ± 0.06	0.29 ± 0.02	0.30
C^+	11.9995	3.31 ± 0.57	0.77 ± 0.02	4.70
O^+	15.9944	0.46 ± 0.15	0.08 ± 0.04	1.70
CO^+	**27.9944**	**100.0 ± 5.1**	**100.0 ± 1.4**	**100.0**
$^{13}CO^+$	28.9977	1.14 ± 0.22	1.21 ± 0.05	1.20
C^+	11.9995	0.44 ± 0.02	1.20 ± 0.10	8.71
O^+	15.9944	10.45 ± 0.24	5.07 ± 0.22	9.61
CO_2^{++}	21.9944	0.25 ± 0.07	0.75 ± 0.05	1.90
CO^+	27.9944	9.73 ± 0.25	3.86 ± 0.21	9.81
$^{13}CO^+$	28.9977	0.09 ± 0.03	0.06 ± 0.08	0.10
CO_2^+	**43.9893**	**100.0 ± 2.5**	**100.0 ± 2.2**	**100.0**
$^{13}CO_2^+$	44.9926	1.23 ± 0.12	1.35 ± 0.14	1.20
$C^{18}OO^+$	46.0049	0.38 ± 0.07	0.39 ± 0.07	0.40
$^4He^+$	**4.0021**	**100.0**	**100.0**	**100.0**
$^{20}Ne^+$	**19.9919**	**100.0 ± 1.7**	**100.0 ± 1.3**	**100.0**
$^{21}Ne^+$	20.9933	0.34 ± 0.08	0.27 ± 0.06	0.30
$^{22}Ne^+$	21.9908	10.94 ± 0.88	10.72 ± 1.02	10.22
$^{40}Ar^{++}$	19.9806	0.04 ± 0.02	10.06 ± 0.12	14.62
$^{36}Ar^+$	35.9670	0.26 ± 0.06	0.31 ± 0.03	0.30
$^{38}Ar^+$	37.9622	0.05 ± 0.02	0.05 ± 0.01	0.05
$^{40}Ar^+$	**39.9618**	**100.0 ± 2.5**	**100.0 ± 1.6**	**100.0**
$^{80}Kr^{++}$	39.9576	∅	0.58 ± 0.12	∅
$^{82}Kr^{++}$	40.9562	0.03 ± 0.02	3.03 ± 0.28	3.47
$^{83}Kr^{++}$	41.4565	0.04 ± 0.02	2.80 ± 0.21	∅
$^{84}Kr^{++}$	41.9552	0.14 ± 0.06	15.11 ± 0.78	15.90
$^{86}Kr^{++}$	42.9548	0.05 ± 0.02	4.46 ± 0.37	4.98
$^{78}Kr^+$	77.9198	0.63 ± 0.01	∅	0.62
$^{80}Kr^+$	79.9158	4.07 ± 0.10	4.03 ± 0.27	4.01
$^{82}Kr^+$	81.9129	20.33 ± 0.33	20.65 ± 0.35	20.34
$^{83}Kr^+$	82.9136	20.18 ± 0.30	20.52 ± 0.36	20.18
$^{84}Kr^+$	**83.9109**	**100.0 ± 1.84**	**100.0 ± 2.0**	**100.0**
$^{86}Kr^+$	85.9101	29.92 ± 0.47	30.79 ± 0.70	30.32
$^{128}Xe^{++}$	63.9512	0.02 ± 0.01	1.36 ± 0.33	∅
$^{129}Xe^{++}$	64.4518	0.31 ± 0.05	19.92 ± 0.78	∅
$^{130}Xe^{++}$	64.9512	0.05 ± 0.01	2.84 ± 0.09	2.93
$^{131}Xe^{++}$	65.4520	0.24 ± 0.04	15.96 ± 0.23	∅
$^{132}Xe^{++}$	65.9515	0.31 ± 0.03	20.25 ± 1.83	17.76
$^{134}Xe^{++}$	66.9521	0.12 ± 0.02	7.88 ± 0.17	6.90
$^{136}Xe^{++}$	67.9531	0.10 ± 0.02	6.54 ± 0.23	6.05
$^{124}Xe^+$	123.9053	0.34 ± 0.08	0.31 ± 0.12	0.35
$^{126}Xe^+$	125.9037	0.30 ± 0.05	0.26 ± 0.11	0.33
$^{128}Xe^+$	127.9030	7.27 ± 0.54	7.28 ± 0.40	7.10
$^{129}Xe^+$	128.9042	97.22 ± 3.15	99.17 ± 2.49	98.11
$^{130}Xe^+$	129.9030	14.95 ± 0.66	15.49 ± 0.46	15.13
$^{131}Xe^+$	130.9045	78.88 ± 2.81	77.15 ± 2.44	78.91
$^{132}Xe^+$	**131.9036**	**100.0 ± 3.9**	**100.0 ± 2.4**	**100.0**
$^{134}Xe^+$	133.9048	39.66 ± 1.81	38.62 ± 1.04	38.78
$^{136}Xe^+$	135.9067	33.47 ± 1.71	32.09 ± 1.28	32.92

The large error bar on the carbon monoxide as a parent (5.1%) reflects a possible contamination by molecular nitrogen from the atmosphere in the analysed sample.

3.1.2. Noble gases

Singly charged ions

Only the most abundant isotope of helium, ^{4}He, can be detected by RTOF: with a relative abundance compared to ^{4}He of $1.34{\cdot}10^{-6}$, even the second most abundant isotope, ^{3}He, is below the actual detection limit of RTOF.

For the heavier noble gases, the isotopic ratios are measured by RTOF with an average accuracy of 2.7% for SS and of 8% for OS. Fig. 8 shows the deviation of the isotopic abundances of Ne, Ar, Kr, and Xe to the literature; the abundances are normalized to the most abundant isotope – ^{20}Ne for Ne, ^{40}Ar for Ar, ^{84}Kr for Kr, and ^{132}Xe for Xe – giving a ratio of 1 for the latter.

The three stable neon isotopes (^{20}Ne, ^{21}Ne, and ^{22}Ne) as well as the three stable argon isotopes (^{36}Ar, ^{38}Ar, and ^{40}Ar) are detected by RTOF, with values close to the standard abundances given by Meija et al. (2016); the large error bars for the least abundant isotopes reflect the small amount of ions observed for these masses.

Regarding the isotopic ratios of krypton, the abundances of the singly charged ions are consistent with the isotopic abundances derived from the CIAAW database, with deviations in the order of a few percent. The signature of ^{78}Kr in the OS data was too low to be quantified in this work.

Finally, the xenon abundances measured here are in good agreement with the literature as well, deviating by only a few percent except for the isotopes with the lowest intensities, i.e. ^{124}Xe and ^{126}Xe. The lager error bars of these two isotopes are once more due to the low signal measured for these two masses.

Doubly charged ions

The amount of doubly charged ions differ significantly between the SS and the OS: this is particularly clear for the noble gases where almost no doubly charged ions are detected for the SS, but a significant amount is seen with the OS. Fig. 9 shows the correlation between the mass and the ratio of doubly to singly charged ions, for the noble gases. The same correlation applies with the ionization cross section, but the mass was chosen to appear on the x-axis to avoid the overlap of the data points for each isotopes.

3.2. Sensitivity

Results for the sensitivity as defined in Eq. (9) are presented in Table 5, for the modes SS – M0521 and OS – M0523. Sensitivities for the other modes may be calculated with the help of the multiplication factors given in Table 6; these factors have been computed thanks to measurements performed specifically with each modes, except for the modes with a 400 s integration time (SS: M0522 and M0527; OS: M0524 and M0554), for which the factor was derived from the modes with equivalent parameters but with a 200 s integration time (SS: M0521 and M0526; OS: M0523 and M0553).

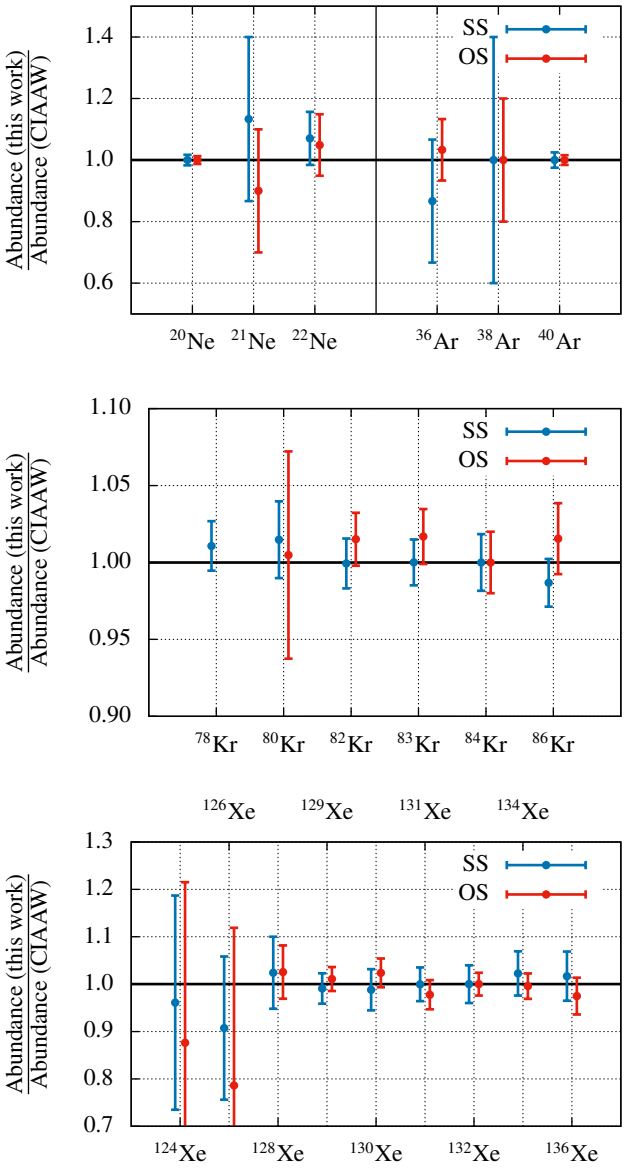

Figure 8: Ratio of the isotopic abundances measured in this work to the isotopic abundances evaluated by the CIAAW (Meija et al., 2016), for the neon and the argon isotopes (top), the krypton isotopes (middle), and the xenon isotopes (bottom).

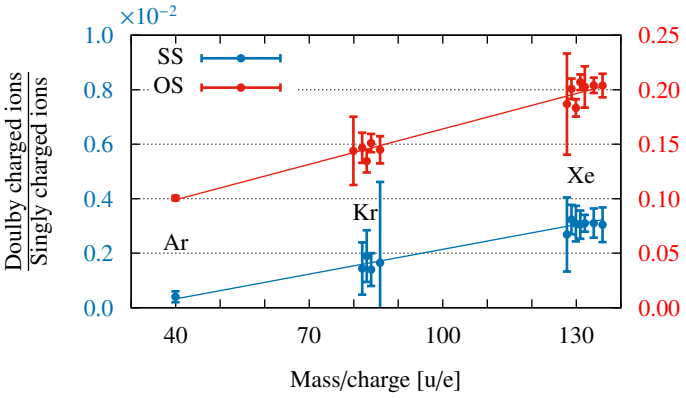

Figure 9: Correlation between mass and doubly/singly charged ions ratio, for the SS and the OS, and for the noble gases Ar, Kr, and Xe.

Table 5: Sensitivities for the modes SS – M0521 (events) and OS – M0523 (events). These two modes have been chosen as references, as they are the modes used the most in flight. Sensitivities for the SS histogram data are on average (20.5 ± 1.5) times higher.

Species	Sensitivity [cm^3]	
	SS	OS
H_2O	$(3.35 \pm 0.14) \cdot 10^{-23}$	$(5.73 \pm 0.66) \cdot 10^{-21}$
CO	$(9.03 \pm 0.80) \cdot 10^{-23}$	$(5.03 \pm 0.58) \cdot 10^{-21}$
CO_2	$(1.40 \pm 0.28) \cdot 10^{-22}$	$(6.84 \pm 0.69) \cdot 10^{-21}$
He	$(4.21 \pm 0.16) \cdot 10^{-24}$	$(2.42 \pm 0.40) \cdot 10^{-22}$
Ne	$(1.73 \pm 0.35) \cdot 10^{-23}$	$(4.37 \pm 0.79) \cdot 10^{-22}$
Ar	$(1.09 \pm 0.22) \cdot 10^{-22}$	$(9.59 \pm 1.41) \cdot 10^{-21}$
Kr	$(1.60 \pm 0.02) \cdot 10^{-22}$	$(1.05 \pm 0.16) \cdot 10^{-20}$
Xe	$(1.48 \pm 0.30) \cdot 10^{-22}$	$(1.73 \pm 0.26) \cdot 10^{-20}$

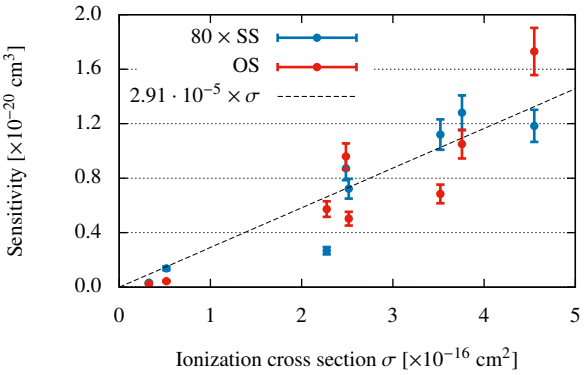

Figure 10: RTOF SS and OS sensitivities with respect to the cross sections of the studied species. Cross sections for H_2O, CO and CO_2 are from Kim et al. (2005), cross sections for the noble gases are from Szmytkowski et al. (1996).

Table 6: Sensitivity conversion factors for the SS and the OS modes (events). Sensitivities for the SS histogram data are on average (20.5 ± 1.5) times higher. A few characteristics of the modes listed below are given in Table 2.

Mode	Conversion factor
SS – M0501	0.118 ± 0.032
SS – M0511	0.229 ± 0.062
SS – M0521	**1.000**
SS – M0522	2.000
SS – M0506	0.068 ± 0.012
SS – M0516	0.499 ± 0.135
SS – M0526	0.112 ± 0.030
SS – M0527	0.224 ± 0.060
OS – M0513	0.116 ± 0.001
OS – M0523	**1.000**
OS – M0524	2.000
OS – M0543	0.059 ± 0.001
OS – M0553	0.517 ± 0.009
OS – M0554	1.034 ± 0.018

The expected linear trend between sensitivity and cross sections is shown in Fig. 10. Although not perfect, the expected correlation between sensitivity and ionization cross section is clear. Total ionization cross sections can therefore be used for first order spectral deconvolution when laboratory data for particular gas species are not available.

4. Application to space data

To demonstrate the capabilities of RTOF in terms of sensitivity, we study here a typical spectrum acquired in space using the Gas Calibration Unit (GCU) of RTOF (see Fig. 2). The GCU is a gas storage reservoir with a well known gas mixture of one third each – by number – of helium, carbon dioxide, and krypton, that can be introduced into the RTOF ion sources in a control way. The GCU is mainly used in flight to record reference mass spectra (see also Section 2.8.1). The spectrum was acquired with OS on 7 January 2015, at 26 km from 67P/C-G's surface, with an electron emission of I_{em} = 200 μA and an extraction frequency of 10 kHz (equivalent to the mode OS – M0523).

The GCU spectrum was fitted using only the intensities of the parent molecules and a global mass-dependent FWHM as fitting parameters (see Fig. 11); the intensities of the fragments are given by the fragmentation pattern and isotopic ratios presented in Table 4.

The analysis of this mass spectrum with sensitivities and fragmentation patterns calibrated on the ground, i.e. the fitting and the numerical integration as described in Section 2, yield the results presented in Table 7: the model fits the data well, with typical fit errors for the intensities in the order of 3%. In terms of sensitivity, the expected fraction of 33.3% for the three calibration species lies within the error bars of the calculated values.

Table 7: Example of density calculations using the calibration values presented in this work. H_2O has a cometary origin and is not part of the GCU gases. The total abundance of H_2O was based on the intensity of the peak at mass 18.0100, the one from CO_2 was based on the intensity of the peak at mass 43.9893, and the one from krypton was based on the intensity of the ^{84}Kr isotope at mass 83.9109.

Compound	c_i [ions]	$f_{i\to j}$	n_i [cm^{-3}]	Fraction [%]
He	8708	1.00	$(2.88 \pm 0.23) \cdot 10^{10}$	**34.4 ± 2.8**
H_2O	425	0.75	$(7.87 \pm 0.63) \cdot 10^{7}$	0.09 ± 0.01
CO_2	207344	0.89	$(2.73 \pm 0.22) \cdot 10^{10}$	**32.7 ± 2.7**
Kr	178281	0.49	$(2.75 \pm 0.22) \cdot 10^{10}$	**32.9 ± 2.7**

5. Conclusion

This work initiates the creation of a database for RTOF with the main components to be expected around 67P/C-G along with noble gases. Divergences in the abundances of fragment peaks with the literature confirm the necessity to have an instrument specific database for the analysis of data collected with RTOF in space: although the fragmentation patterns of H_2O, CO, and CO_2 follow roughly the same trends as NIST,

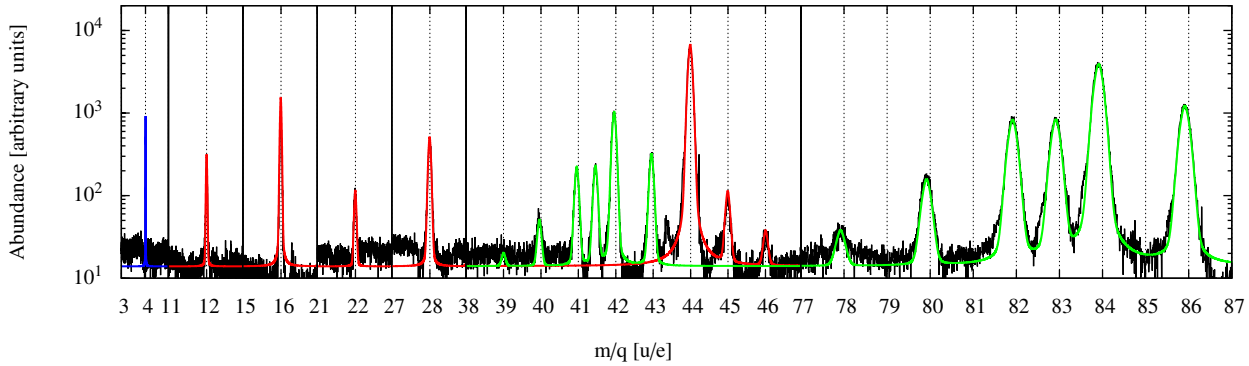

Figure 11: GCU spectrum with its model generated with the fragmentation patterns of 4 compounds: He (blue), H_2O (not shown here), CO_2 (red), and Kr (green). Only parts of the spectrum are displayed for clarity reasons.

the details of the patterns differ. On the other hand, the isotopic ratios for the noble gases as well as the abundance of the isotopologues for each molecules are consistent with the literature, with error bars in the order of a few percent.

Regarding the sensitivities, the expected correlation with the ionization cross section has been verified, but confirms at the same time that species-specific calibration measurements are essential for the accurate computation of densities.

Ultimately, it has been demonstrated that despite two technical failures in flight, RTOF is still fully capable of identifying the gaseous compounds in its surrounding using the fragmentation data from this calibration campaign, and to quantify the density of the gases entering its sources using the calibrated sensitivities.

6. Acknowledgments

The authors thank the following institutions and agencies, which supported this work. Work at the University of Bern was funded by the State of Bern, the Swiss National Science Foundation, and the European Space Agency PRODEX Program. Work at the Max Planck Institute for Solar System Research was funded by the Max-Planck Society and Bundesministerium für Wirtschaft und Energie under contract 50QP1302. This work was supported by CNES grants at IRAP. Work by J.H.W. at the Southwest Research Institute was funded by NASA JPL subcontract NAS703001TONMO710889. The results from ROSINA would not be possible without the work of the many engineers, technicians, and scientists involved in the mission, in the Rosetta spacecraft, and in the ROSINA instrument team over the past 20 years, whose contributions are gratefully acknowledged. Rosetta is an European Space Agency (ESA) mission with contributions from its member states and NASA. We thank herewith the work of the whole ESA Rosetta team. All ROSINA flight data have been / will be released to the PSA archive of ESA and to the PDS archive of NASA.

7. References

Abplanalp, D., Wurz, P., Huber, L., Leya, I., 2010. An optimised compact electron impact ion storage source for a time-of-flight mass spectrometer. International Journal of Mass Spectrometry 294 (1), 33–39.

Altwegg, K., Balsiger, H., Bar-Nun, A., Berthelier, J. J., Bieler, A., Bochsler, P., Briois, C., Calmonte, U., Combi, M., De Keyser, J., Eberhardt, P., Fiethe, B., Fuselier, S., Gasc, S., Gombosi, T. I., Hansen, K. C., Hässig, M., Jäckel, A., Kopp, E., Korth, A., LeRoy, L., Mall, U., Marty, B., Mousis, O., Neefs, E., Owen, T., Rème, H., Rubin, M., Sémon, T., Tzou, C.-Y., Waite, H., Wurz, P., Jan. 2015. 67P/Churyumov-Gerasimenko, a Jupiter family comet with a high D/H ratio. Science 347 (27), A387.

Balsiger, H., Altwegg, K., Bochsler, P., Eberhardt, P., Fischer, J., Graf, S., Jäckel, A., Kopp, E., Langer, U., Mildner, M., Müller, J., Riesen, T., Rubin, M., Scherer, S., Wurz, P., Wüthrich, S., Arijs, E., Delanoye, S., de Keyser, J., Neefs, E., Nevejans, D., Rème, H., Aoustin, C., Mazelle, C., Médale, J.-L., Sauvaud, J. A., Berthelier, J.-J., Bertaux, J.-L., Duvet, L., Illiano, J.-M., Fuselier, S. A., Ghielmetti, A. G., Magoncelli, T., Shelley, E. G., Korth, A., Heerlein, K., Lauche, H., Livi, S., Loose, A., Mall, U., Wilken, B., Gliem, F., Fiethe, B., Gombosi, T. I., Block, B., Carignan, G. R., Fisk, L. A., Waite, J. H., Young, D. T., Wollnik, H., Feb. 2007. Rosina Rosetta Orbiter Spectrometer for Ion and Neutral Analysis. Space Science Reviews128, 745–801.

Bieler, A., Altwegg, K., Balsiger, H., Bar-Nun, A., Berthelier, J.-J., Bochsler, P., Briois, C., Calmonte, U., Combi, M., De Keyser, J., van Dishoeck, E. F., Fiethe, B., A. Fuselier, S. A., Gasc, S., Gombosi, T., Hansen, K. C., Hässig, M., Jäckel, A., Kopp, E., Korth, A., Le Roy, L., Mall, U., Maggiolo, R., Marty, B., Mousis, O., Owen, T., Rème, H., Rubin, M., Sémon, T., Tzou, C.-Y., Waite, J. H., Walsh, C., Wurz, P., Oct. 2015. Abundant molecular oxygen in the coma of comet 67P/Churyumov-Gerasimenko. Nature526, 678–681.

Bieler, A., Altwegg, K., Hofer, L., Jäckel, A., Riedo, A., Sémon, T., Wahlström, P., Wurz, P., 2011. Optimization of mass spectrometers using the adaptive particle swarm algorithm. Journal of Mass Spectrometry 46 (11), 1143–1151.

Bockelée-Morvan, D., Crovisier, J., Mumma, M. J., Weaver, H. A., 2004. The composition of cometary volatiles. pp. 391–423.

Graf, S., Altwegg, K., Balsiger, H., Jäckel, A., Kopp, E., Langer, U., Luithardt, W., Westermann, C., Wurz, P., May 2004. A cometary neutral gas simulator for gas dynamic sensor and mass spectrometer calibration. Journal of Geophysical Research (Planets) 109, 7.

Granville-Phillips, 2007. Granville-Phillips Series 370 Stabil-Ion® Vacuum Measurement Controller Instruction Manual, revision 05.

Hässig, M., Altwegg, K., Balsiger, H., Bar-Nun, A., Berthelier, J. J., Bieler, A., Bochsler, P., Briois, C., Calmonte, U., Combi, M., De Keyser, J., Eberhardt, P., Fiethe, B., Fuselier, S. A., Galand, M., Gasc, S., Gombosi, T. I., Hansen, K. C., Jäckel, A., Keller, H. U., Kopp, E., Korth, A., Kührt, E., Le Roy, L., Mall, U., Marty, B., Mousis, O., Neefs, E., Owen, T., Rème, H., Rubin, M., Sémon, T., Tornow, C., Tzou, C.-Y., Waite, J. H., Wurz, P., Jan. 2015. Time variability and heterogeneity in the coma of 67P/Churyumov-Gerasimenko. Science 347 (1), aaa0276.

Kim, Y.-K., Irikura, K., Rudd, M., Ali, M., Stone, P., Chang, J., Coursey, J., Dragoset, R., Kishore, A., Olsen, K., Sansonetti, A., Wiersma, G., Zucker, D., M.A., Z., 2005. Electron-impact cross section database. NIST Standard Reference Database 107.

Mall, U., Altwegg, K., Balsiger, H., Bar-Nun, A., Berthelier, J.-J., Bieler, A., Bochsler, P., Briois, C., Calmonte, U., Combi, M. R., Dabrowski, B., De Keyser, J., Dhooghe, F., Fiethe, B., Fuselier, S. A., Galli, A., Garnier, P., Gasc, S., Gombosi, T. I., Hansen, K. C., Hässig, M., Hoang, M., Jäckel, A.,

Kopp, E., Korth, A., Le Roy, L., Magee, B., Marty, B., Mousis, O., Rème, H., Rubin, M., Sémon, T., Tzou, C.-Y., Waite, J. H., Wurz, P., Mar. 2016. High-Time Resolution In-situ Investigation of Major Cometary Volatiles around 67P/C-G at 3.1 - 2.3 AU Measured with ROSINA-RTOF. Astrophysical Journal819, 126.

Mamyrin, B., Karataev, V., Shmikk, D., Zagulin, V., 1973. The mass-reflectron, a new non-magnetic time-of-flight mass spectrometer with high resolution. Zh. Eksp. Teor. Fiz 64, 82–89.

Mark, T., 1982. Fundamental aspects of electron impact ionization. International Journal of Mass Spectrometry and Ion Physics 45, 125–145.

Meija, J., Coplen, T. B., Berglund, M., Brand, W. A., De Bièvre, P., Gröning, M., Holden, N. E., Irrgeher, J., Loss, R. D., Walczyk, T., et al., 2016. Isotopic compositions of the elements 2013 (iupac technical report). Pure and Applied Chemistry 88 (3), 293–306.

Mumma, M. J., Charnley, S. B., Sep. 2011. The Chemical Composition of Comets—Emerging Taxonomies and Natal Heritage. Annual Review of Astronomy and Astrophysics49, 471–524.

Owen, T., Bar-Nun, A., Kleinfeld, I., Jul. 1992. Possible cometary origin of heavy noble gases in the atmospheres of Venus, earth, and Mars. Nature358, 43–46.

Riedo, A., Bieler, A., Neuland, M., Tulej, M., Wurz, P., 2013. Performance evaluation of a miniature laser ablation time-of-flight mass spectrometer designed for in situ investigations in planetary space research. Journal of Mass Spectrometry 48 (1), 1–15.

Rubin, M., Altwegg, K., Balsiger, H., Bar-Nun, A., Berthelier, J.-J., Bieler, A., Bochsler, P., Briois, C., Calmonte, U., Combi, M., De Keyser, J., Dhooghe, F., Eberhardt, P., Fiethe, B., Fuselier, S. A., Gasc, S., Gombosi, T. I., Hansen, K. C., Hässig, M., Jäckel, A., Kopp, E., Korth, A., Le Roy, L., Mall, U., Marty, B., Mousis, O., Owen, T., Rème, H., Sémon, T., Tzou, C.-Y., Waite, J. H., Wurz, P., Apr. 2015. Molecular nitrogen in comet 67P/Churyumov-Gerasimenko indicates a low formation temperature. Science 348, 232–235.

Scherer, S., Altwegg, K., Balsiger, H., Fischer, J., Jäckel, A., Korth, A., Mildner, M., Piazza, D., Reme, H., Wurz, P., 2006. A novel principle for an ion mirror design in time-of-flight mass spectrometry. International Journal of Mass Spectrometry 251 (1), 73–81.

Schläppi, B., Altwegg, K., Balsiger, H., Hässig, M., Jäckel, A., Wurz, P., Fiethe, B., Rubin, M., Fuselier, S. A., Berthelier, J. J., de Keyser, J., Rème, H., Mall, U., Dec. 2010. Influence of spacecraft outgassing on the exploration of tenuous atmospheres with in situ mass spectrometry. Journal of Geophysical Research (Space Physics) 115, A12313.

Schletti, R., Wurz, P., Scherer, S., Siegmund, O. H., 2001. Fast microchannel plate detector with an impedance matched anode in suspended substrate technology. Review of Scientific Instruments 72 (3), 1634–1639.

Stein, S., 2013. NIST Mass Spec Data Center, "Mass Spectra" in NIST Chemistry WebBook, NIST Standard Reference Database Number 69.

Szmytkowski, C., Maciag, K., Karwasz, G., 1996. Absolute electron-scattering total cross section measurements for noble gas atoms and diatomic molecules. Physica Scripta 54, 271–280.

Wang, M., Audi, G., Wapstra, A., Kondev, F., MacCormick, M., Xu, X., Pfeiffer, B., 2012. The Ame2012 atomic mass evaluation. Chinese Physics C 36 (12), 1603.

Wurz, P., Balogh, A., Coffey, V., Dichter, B. K., Kasprzak, W. T., Lazarus, A. J., Lennartsson, W., McFadden, J. P., 2007. Calibration Techniques. ISSI Scientific Reports Series 7, 117–276.